Phase-Encoded Linear Sampling Method Imaging of Conducting Surfaces From Full and Limited Synthetic Apertures

MATTHEW J. BURFEINDT (Member, IEEE), AND HATIM F. ALQADAH

Radar Division, U.S. Naval Research Laboratory, Washington, DC 20375, USA

CORRESPONDING AUTHOR: M. J. BURFEINDT (e-mail: matthew.burfeindt@nrl.navy.mil)

ABSTRACT The linear sampling method (LSM) is a qualitative inverse scattering technique that can create good-fidelity imagery at low computational expense. However, it is challenging to use in many practical scenarios due to its need for wide-angle multistatic-multiview data with dense spatial sampling. We present a new LSM formulation for imaging conducting targets from a more limited sensor distribution. The technique mitigates the challenge of limited multistatic diversity by disciplining the solution via a propagation-based phase encoding. Phase encoding is accomplished on receive via a beamforming operation and on transmit via a regularization that enforces a desired phase behavior. We evaluate the method by applying it to multistatic synthetic aperture scenarios where a few sensors travel in formation while collecting data. These scenarios are challenging for conventional LSM, but also potentially desirable due to the limited required hardware resources. We demonstrate with both simulated and experimental data that the proposed technique produces images of fundamentally greater fidelity compared to conventional LSM processing. We demonstrate significantly improved performance both when the aperture completely encircles the target and when the aperture is limited in aspect. The latter result is particularly significant, as limited apertures present significant challenges to LSM imaging.

INDEX TERMS Inverse scattering, beamforming, antenna arrays.

I. INTRODUCTION

INVERSE scattering techniques are of interest for a variety of applications related to sensing of conducting targets, including target identification, target classification, and non-destructive evaluation. Such techniques belong to two broad categories. *Quantitative* techniques (e.g., [1], [2], [3]) reconstruct the dielectric profile of the target, typically through the use of nonlinear optimization. *Qualitative* techniques reconstruct only the target shape and neglect the target's constituent dielectric properties. For targets that are known to be perfect electric conductors (PECs) or near-PECs, as would be expected for many types of man-made objects, qualitative methods have several advantages relative to quantitative methods. Quantitative methods such as the Born iterative method [1] and the distorted Born iterative method [2] often struggle for high-contrast targets or take many iterations. In addition, the sensitivity of quantitative methods to forward

solution error presents challenges when there are mismatches between the true and assumed propagation environments (e.g., [4]). Lastly, the internal dielectric profile of a near-PEC target is generally non-informative, and thus the computational expense associated with performing a quantitative estimate via nonlinear optimization may not be justified.

Various qualitative imaging algorithms have been formulated specifically for PEC targets or have been applied to PEC targets in previous studies. Local shape function and subspace optimization methods discretize the imaging domain into small conducting elements and then use nonlinear optimization to determine which elements compose the target [5], [6], [7], [8], [9], [10]. Several techniques solve for the locations of equivalent sources on the PEC surface via optimization with spatial sparsity assumptions [11], [12], [13], [14], [15], [16]. Techniques based on physical optics use high-frequency approximations to

simplify the reconstruction [17], [18], [19]. The direct sampling method (DSM) (e.g., [20], [21]) and the orthogonal sampling method (OSM) (e.g., [22], [23]) generate indicator functions using the inner product of the scattered field and the Green's function at each image pixel.

Among the various qualitative techniques, the linear sampling method (LSM) in particular has received a considerable amount of attention due to several beneficial properties [24], [25], [26], [27], [28], [29], [30], [31], [32], [33], [34], [35], [36], [37], [38], [39]. The LSM operates by solving a linear focusing problem [25], and thus is computationally inexpensive and straightforward to implement. In addition, in its conventional formulation, it does not rely on the Born or weak-scattering approximation, and thus can create images of good fidelity.

However, practical LSM imaging is challenging due to its need for spatially dense and wide-angle multistatic-multiview (MMV) data. In most LSM studies, the target is surrounded on all sides by a dense array of transmit locations and a perhaps co-located dense array of receive locations. Electric field data are collected for each transmit-receive location combination, resulting in a rich multistatic set of electric field phasors at every frequency. If data are collected without considerable transmit-receive angular diversity, then the LSM in its conventional formulation is expected to suffer from a significant loss of image fidelity. The required sensor density may be prohibitive for many applications due to the cost of resources or data acquisition time. The challenge grows considerably as the frequency of operation increases, as the number of spatial samples increases with the electrical size of the target [25]. Perhaps partially for this reason, most LSM studies assume targets that are only a few wavelengths in size.

Limited-aperture scenarios, in which sensors are placed on only one side of the target, are well-known to be particularly challenging for the conventionally formulated LSM. Target responses in conventional LSM imagery from limited apertures are often very aberrant or significantly elongated in the direction orthogonal to the arrays, i.e., the range direction in radar parlance. This loss of fidelity can occur even when the limited aperture is densely sampled on both transmit and receive. The LSM struggles to discriminate in the range direction of a limited aperture principally because much of the signal range information is related to the change of the phase across frequency. The conventional multifrequency LSM lacks a mechanism for exploiting this phase change and instead typically operates by combining the single-frequency images non-coherently, which is less effective if there is a lack of angular diversity in sensor placement.

Limited-aperture LSM imaging has been studied for cases where there is a free-space path from the sensors to the target [32], [33], [34], [35] as well as for cases where the target is embedded beneath a penetrable surface [36], [37], [38], [39], [40]. We focus on the former case in this paper, which is consistent with many past PEC imaging studies [5], [6], [7], [8], [9], [10], [11], [12], [14], [15],
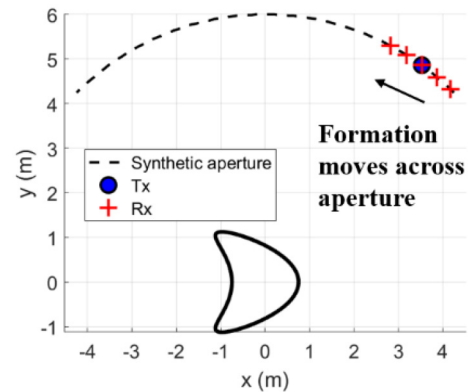

FIGURE 1. An illustration of the multistatic synthetic aperture data collection scenario of interest. In this study, we use both the 90° synthetic aperture depicted as well as a 360° synthetic aperture.

[16], [17], [18], [19], [20], [21], [22], [23]. Various strategies have been studied for overcoming the limited-aperture challenge, including applying an amplitude weighting on the right-hand-side of the LSM system of equations [36], [38], using a time-domain LSM implementation [32], [33], and using a regularization term related to the factorization of the far-field operator [35].

In this paper, we present a new LSM formulation for imaging conducting targets with limited sensors. To mitigate a lower-than-desired degree of MMV diversity, the new technique disciplines the LSM reconstruction by encoding phase information on both transmit and receive, and thus we refer to it as the phase-encoded LSM (PE-LSM). The PE-LSM encodes *receive* phase information by applying a receive beamforming operation to focus the receive array at each imaging scene pixel prior to finding the LSM solution. The PE-LSM encodes *transmit* phase information by enforcing a propagation-based phase constraint on the LSM solution via phase-delay frequency variation (PDFV) regularization [29]. The PDFV regularization links the phase of the LSM solution across frequency according to the propagation delay. This incorporates *a priori* information into the optimization that can mitigate the lack of spatial measurements. Linking the solution phase across frequency in this way also allows the PE-LSM to leverage signal range information to a greater extent than the conventional LSM.

We investigate the proposed PE-LSM formulation in a scenario that is challenging for conventional LSM processing but attractive from a practical perspective. The chosen scenario, illustrated in Figure 1, uses a few sensors (in this case, a single transmitter and five receivers) that move in formation across a synthetic aperture while collecting multistatic data at regular pulse repetition intervals. This multistatic synthetic aperture approach is attractive, as it allows for collecting data with only a handful of physical sensors while achieving significant azimuthal diversity for monostatic and near-monostatic samples. In addition, the synthetic aperture approach allows for dense spatial sampling even for electrically large targets through the use of a short pulse repetition

interval, and thus may allow for imaging of electrically large targets via the capture of higher spatial frequencies. However, as receive samples are limited to the close vicinity of the transmit location, achieving high-fidelity imagery from conventional LSM processing is still difficult. A similar synthetic aperture approach has been used for LSM in a few studies [34], [38], [40]. However, the overwhelming majority of LSM studies have not used this approach, and thus more extensive study is of interest. Of particular interest are results against electrically large targets, which as stated previously are less common in the LSM literature.

We show that the PE-LSM generates good-fidelity imagery for multistatic synthetic apertures that completely encircle the target as well for the much more challenging scenario where the synthetic aperture is limited in aspect. The technique accurately reconstructs not only the target location but also the shapes of the target surfaces that are illuminated by the sensors. We show that imaging performance for the PE-LSM is fundamentally improved over conventional LSM processing. In addition, we show that good-fidelity imaging requires the use of both the receive and transmit encoding in concert, whereas use of only one or the other results in limited fidelity.

We have previously presented preliminary imaging results for this method in a brief conference paper [31], wherein we demonstrate imaging efficacy for a simulated limited-aperture scenario with dense transmit samples and sparse stationary receive samples. The work in this paper provides a more comprehensive investigation of performance, including a study on the choice of regularization parameters, a wider array of simulated targets, and an experimental example. In addition, this paper focuses on the synthetic aperture sensor configuration, which as stated previously allows for the imaging of electrically larger targets with only a few sensors.

The work in this study is distinct from our previous work on sparse-aperture LSM imaging. In [29], we first formulated the PDFV method and applied it to wide-angle sparse-receive scenarios. However, the receive beamforming enhancement was not included, which as is shown in this paper is necessary for imaging in the challenging multistatic synthetic aperture scenario of interest. In [30], we formulated a sparse-receive LSM technique for conducting targets that leveraged electric field boundary conditions. However, unlike the PE-LSM technique, this boundary-condition-enhanced LSM relies on iterative nonlinear optimization, and thus is significantly more computationally expensive.

Lastly, the PE-LSM is also distinct from non-LSM algorithms presented in past work for imaging conducting targets. It does not require iterative, nonlinear optimization, as do local shape function and subspace optimization techniques [5], [6], [7], [8], [9], [10]. It does not explicitly rely on an assumption of sparsity in the unknown contrast, as in [11], [12], [13], [14], [15], [16]. In addition, it is effective in multistatic synthetic aperture scenarios, which to our knowledge have not been explored extensively for these previously reported techniques.

The remainder of this paper are organized as follows. In Section II, we describe the formulation of the PE-LSM method. In Section III, we evaluate performance across a wide variety of imaging results, including results from simulated datasets as well as a publicly available limited-aspect experimental example. Finally, we make summary statements in the Conclusion.

II. IMAGING FORMULATION
A. CONVENTIONAL LSM FORMULATION
The standard LSM involves solving a system of linear equations for each imaging scene pixel and each collected frequency. The solution of the linear system, which is in the form of a weighting on the incident field from each transmitter, is then used to calculate an indicator function at each pixel which takes on different values for pixels that are inside or outside the target support. We detail our implementation of the standard LSM as follows.

For ease of explication, we assume a 2D imaging scene and transverse-magnetic propagation. We assume an unknown target is surrounded by N_{tx} transmit locations and N_{rec} receive locations. The scattered electric field phasors at free-space wavenumber k for every multistatic combination of transmit and receive location are collected into the $N_{rec} \times N_{tx}$ matrix $\mathbf{E}(k)$. To form an image using the conventional LSM formulation, we first solve the following system of linear equations,

$$\mathbf{E}(k)\mathbf{g}(k, \mathbf{r}) = \mathbf{\Phi}(k, \mathbf{r}), \qquad (1)$$

where $\mathbf{r}$ is a pixel location in the imaging domain, $\mathbf{g}(k, \mathbf{r})$ is the $N_{tx} \times 1$ LSM solution at $\mathbf{r}$, and $\mathbf{\Phi}(k, \mathbf{r})$ is the $N_{rec} \times 1$ vector of Green's functions between $\mathbf{r}$ and each receive location. Solving (1) can be seen as a transmit beamforming problem where a set of complex transmit weights $\mathbf{g}(k, \mathbf{r})$ is chosen to transform $\mathbf{E}(k)$ into the elementary pattern $\mathbf{\Phi}(k, \mathbf{r})$. Thus, solving for $\mathbf{g}(k, \mathbf{r})$ involves finding N_{tx} complex unknowns from N_{rec} observation vectors. A distinct linear system is solved for every individual k of interest and every pixel location $\mathbf{r}$ in the scene.

In this study, we choose a normalized Green's function of the form

$$\mathbf{\Phi}(k, \mathbf{r}) = \mathbf{\Phi}_0(k, \mathbf{r}) / \|\mathbf{\Phi}_0(k, \mathbf{r})\|, \qquad (2)$$

where the ith element of $\mathbf{\Phi}_0(k, \mathbf{r})$ is

$$\Phi_0^i(k, \mathbf{r}) = H_0^2\left(k d_{rec}^i(\mathbf{r})\right), \qquad (3)$$

$H_0^2(\cdot)$ is the zeroth-order Hankel function of the second kind, and $\mathbf{d}_{rec}(\mathbf{r})$ is the $N_{rec} \times 1$ vector of distances between $\mathbf{r}$ and each receive location. Thus, $\mathbf{\Phi}(k, \mathbf{r})$ is a vector whose elements are the conventional Green's function in 2D, divided by its norm.

Normalizing the Green's function vector in the manner of (2) has been shown in previous work [36] to improve limited-aperture performance. We follow this convention, as an aim for this study is to evaluate the PE-LSM in limited aperture geometries.

The imaging problem is ill-posed in general, and thus solving (1) typically requires regularization. The solution at a given k and $\mathbf{r}$ using the common Tikhonov method is given by

$$\min_{\mathbf{g}(k,\mathbf{r})} \|\boldsymbol{\rho}(k,\mathbf{r})\|^2 + \alpha\|\mathbf{g}(k,\mathbf{r})\|^2, \qquad (4)$$

where $\boldsymbol{\rho}(k,\mathbf{r}) = \mathbf{E}(k)\mathbf{g}(k,\mathbf{r}) - \boldsymbol{\Phi}(k,\mathbf{r})$ is the residual function for (1), α is a regularization parameter that controls the influence of the penalty on large-norm solutions, the first norm is across the "receiver" dimension (and thus is across N_{rec} elements), and the second norm is across the "transmit" dimension (and thus is across N_{tx} elements).

It can be shown using mathematical [24] or electromagnetic arguments [25] that, assuming sufficient spatial sampling, the LSM solution will have a low magnitude for pixels inside the target support and a high magnitude for pixels outside the target support. Thus an image of the target can be formed by finding a solution for (4) for every individual $\mathbf{r}$ in the scene and then simply displaying an indicator function of the LSM solution norm $\|\mathbf{g}(k,\mathbf{r})\|$ at each pixel.

Creating indicator functions from multifrequency data acquisitions generally involves solving (4) at all k of interest and then combining the solution norms for each k into a single scalar value for each $\mathbf{r}$. Various multifrequency indicator functions have been used in the literature previously. A common choice is some variation of

$$I(\mathbf{r}) = \sum_i \|\mathbf{g}(k_i,\mathbf{r})\|^{-p}, \qquad (5)$$

where k_i is the ith collected wavenumber and $p = 1$ or 2 (e.g., [28], [32]). Other studies focused on ground penetrating radar (GPR) applications have normalized each frequency component by the maximum over the image in order to overcome challenges related to the differences in penetration distance across frequency [34], [36]. Although the focus of this study is not GPR, we adopt this convention in order to maintain consistency with previously published experimental results [34]. The indicator function we use in this study is given by

$$I(\mathbf{r}) = \left(\sum_i \frac{\|\mathbf{g}(k_i,\mathbf{r})\|^2}{\max_{\mathbf{r}'} \|\mathbf{g}(k_i,\mathbf{r}')\|^2} \right)^{-1}. \qquad (6)$$

This indicator is identical to the indicator used in [34], [36], with the exception that the reciprocal is taken in order to follow the commonly used convention that the indicator is high inside the target support and low outside of it (e.g., [24], [26], [28], [32], [35]).

The preceding development highlights the significant benefits of standard LSM processing. Solving (4) for every pixel and frequency and then combining the solutions into an indicator function via (5) or (6) is both straightforward and computationally inexpensive. However, if there is insufficient diversity in transmit/receive location combinations,

the solution to (4) will fail to evince the desired solution norm behavior, resulting in aberrant imagery. We detail our proposed method for mitigating these problems in the next section.

B. PE-LSM FORMULATION

The PE-LSM formulation includes two primary enhancements to the conventional LSM formulation to enable effective imaging in the challenging synthetic aperture scenarios of interest for this study. First, the LSM problem statement is modified via a receive beamforming operation. Second, the transformed problem is solved using PDFV regularization. Each enhancement is described below.

We implement the receive beamforming enhancement by taking the inner product of both sides of (1) with a beamforming weight vector given by

$$\mathbf{w}(k,\mathbf{r}) = \exp(-jk\mathbf{d}_{\text{rec}}(\mathbf{r})). \qquad (7)$$

The resulting transformed system of equations is

$$\mathbf{w}^{\text{H}}(k,\mathbf{r})\mathbf{E}(k)\mathbf{g}(k,\mathbf{r}) = \mathbf{w}^{\text{H}}(k,\mathbf{r})\boldsymbol{\Phi}(k,\mathbf{r}), \qquad (8)$$

where 'H' refers to the conjugate transpose. The rationale for beamforming with the weight in (7) is that the matched phases backproject the receive data to pixel $\mathbf{r}$, which focuses the receive array such that scattering mechanisms near the pixel are emphasized. We hypothesize that this focusing procedure filters the data in such a way that reduces the complexity of the solution space by ignoring potential scattering contributions of equivalent currents remote from the pixel. The simplification in the problem, i.e., the reduction in the allowable degrees of freedom for the solution, can then stabilize the optimization for the scenario where there are also limited degrees of freedom in the measured data due to a lack of a full complement of MMV sensors, as in the sensor configuration of interest for this paper.

However, proper choice of regularization is still needed to faithfully solve the system. In the PE-LSM formulation, we regularize via the PDFV method which we originally introduced for non-beamformed LSM [29]. The PDFV-regularized solution to (8) is given by

$$\min_{\mathbf{g}(k,\mathbf{r})} \sum_i \left| \mathbf{w}^{\text{H}}(k_i,\mathbf{r})\boldsymbol{\rho}(k_i,\mathbf{r}) \right|^2 + \alpha\|\mathbf{g}(k_i,\mathbf{r})\|^2 + \beta\|\boldsymbol{\gamma}(k_i,\mathbf{r})\|^2. \qquad (9)$$

In (9), $\mathbf{w}^{\text{H}}(k,\mathbf{r})\boldsymbol{\rho}(k,\mathbf{r}) = \mathbf{w}^{\text{H}}(k,\mathbf{r})(\mathbf{E}(k)\mathbf{g}(k,\mathbf{r}) - \boldsymbol{\Phi}(k,\mathbf{r}))$ is the new beamformed residual function for (8),

$$\boldsymbol{\gamma}(k,\mathbf{r}) = \mathbf{g}(k,\mathbf{r}) - \mathbf{g}(k + \Delta k, \mathbf{r}) \odot \exp(-j\Delta k \mathbf{d}_{\text{tx}}(\mathbf{r})) \quad (10)$$

is the PDFV penalty, and α and β are regularization parameters that control the relative influences of the large-norm and PDFV penalties, respectively. In (10), Δk is the spacing between adjacent wavenumbers, $\mathbf{d}_{\text{tx}}(\mathbf{r})$ is the $N_{\text{tx}} \times 1$ vector of distances between $\mathbf{r}$ and each transmitter, and $\odot$ symbolizes element-wise multiplication.
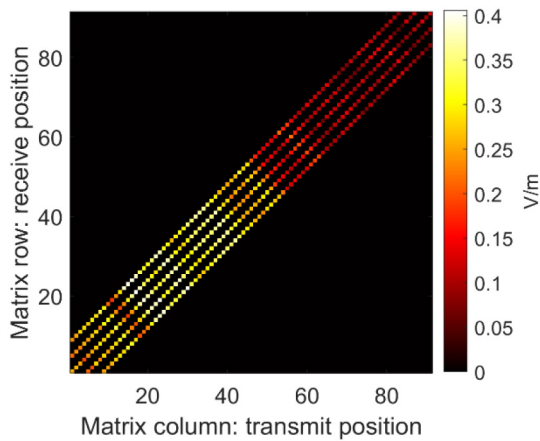
FIGURE 2. The form of the data matrix for the multistatic synthetic aperture scenario. The value displayed for each element is the magnitude of the scattered field phasor.

The PDFV penalty in (10) emphasizes solutions for which the phase difference at adjacent frequencies is approximately equal to the change in electrical path length from the transmitters to $\mathbf{r}$, given by $\Delta k \mathbf{d}_{tx}(\mathbf{r})$. As explained in [29], the rationale for this constraint is related to the perspective of the LSM solution as a set of weights on the transmitters that focus equivalent currents in the target space at $\mathbf{r}$. Linking the solutions across frequency in this way effectively incorporates *a priori* information to the LSM optimization which also mitigates the lack of a full complement of MMV spatial samples.

The minimization in (9) can be accomplished in a straightforward manner by solving a linear system of equations in block-matrix form. The block matrix implementation follows a similar form as described in [29].

C. MULTISTATIC SYNTHETIC APERTURE FORMULATION
The synthetic aperture scenario depicted in Figure 1 is distinct from the imaging scenario used in most LSM studies in that only a few receive samples are collected for every transmit position. To account for this in both the conventional and PE-LSM implementations, we follow a strategy that has been used in previous studies [34], [38], [40]. Assuming that multistatic data are collected for N positions of the sensor formation in the synthetic aperture, then we choose the size of $\mathbf{E}(k)$ to be $N_{rec} \times N_{tx} = N \times N$. We then fill all elements of $\mathbf{E}(k)$ corresponding to transmit-receive combinations that are collected in the imaging scenario and leave the remaining elements as zeros.

An example $\mathbf{E}(k)$ matrix is depicted in Figure 2. The data for the matrix are extracted from a finite-difference time-domain (FDTD) simulation of the kite-shaped target in Figure 1 across a 90° synthetic aperture. Data are collected at 1° increments, resulting in a data matrix of size 90×90. The spacing between adjacent receivers is 4°. For visualization purposes, the color of each displayed element is determined by the amplitude of the collected scattered field phasor for the corresponding transmit-receive combination.

(Of course, in implementing the imaging algorithms, $\mathbf{E}(k)$ is filled with the complex phasors of the scattered field, and not their magnitudes.) Black elements correspond to zeros, i.e., uncollected samples.

As can be seen, $\mathbf{E}(k)$ is in the form of a multi-diagonal matrix. The central diagonal corresponds to the monostatic data from the central transmitter/receiver, while the other four diagonals correspond to the multistatic data for the remaining receivers. Each diagonal is shifted by four elements from its neighbors due to the 4° spacing between the receivers.

III. RESULTS
In this section, we evaluate the performance of the PE-LSM across a variety of imaging examples. In Section III-A, we first describe our procedure for acquiring simulated data. In Section III-B, we explore the effects of the regularization parameters, describe a heuristic for choosing these parameters, and demonstrate basic imaging efficacy. We compare these results to the standard LSM and other LSM variants in Section III-C. We evaluate performance for a wider variety of targets in Section III-D. We then explore the robustness of the PE-LSM to noise and lower conductivity in Section III-E and Section III-F, respectively. We give an experimental imaging example in Section III-G. Finally, we discuss the results in Section III-H.

A. SIMULATED DATA ACQUISITIONS
We generate simulated data for the sensor geometry illustrated in Figure 1 using the 2D FDTD method. We place a target in the imaging scene near the origin of the Cartesian coordinate system. Unless otherwise specified, we choose for the target to have a conductivity of 5.7×10^7 S/m, which is similar to copper. Each simulated target used in this study is around 2 to 3 m in size along its largest dimensions.

We define a synthetic aperture in the form of an arc of radius 6 m. Across various imaging trials, we choose for the synthetic aperture to have an angular extent of 360° (i.e., to completely surround the target) or 90°. In the latter case, the aperture begins at an azimuthal angle of 45° and ends at an azimuthal angle of 135° measured counter-clockwise from the $+x$-axis, as shown in Figure 1.

We sequentially source a series of transmit positions across the synthetic aperture using elementary currents. The transmit positions are uniformly distributed across the synthetic aperture in 1° increments. For each transmit position, we collect the time-domain scattered field at five receive locations on the arc. The formation of receive locations is centered on the transmitter and adjacent receivers are separated by 2°. We then compute frequency-domain phasors for each transmit-receive combination using the discrete Fourier Transform and collect the phasors in matrix $\mathbf{E}(k)$ as described in Section II-C. We choose six frequencies uniformly distributed between 1.5 and 1.6 GHz. At these frequencies, the targets span around 10 to 15 wavelengths along their largest dimensions, and thus are of significant electrical size. We add Gaussian white noise to the phasors such that the total
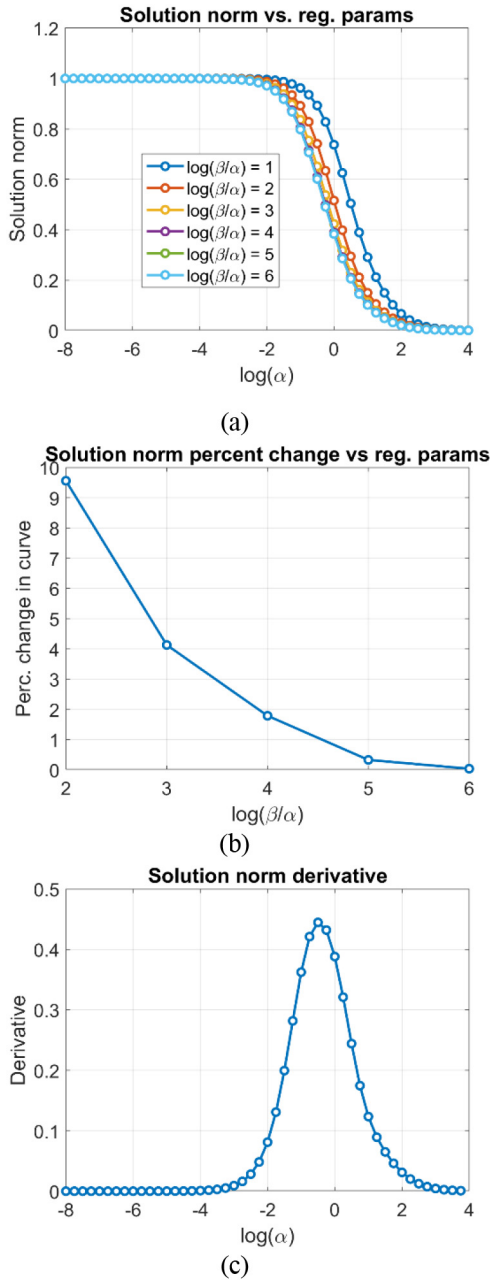
(a)

(b)

(c)

FIGURE 3. (a) The behavior of the PE-LSM solution norm as a function of the regularization parameters. (b) The percent change of the solution norm curves as a function of the ratio of the regularization parameters. (c) The magnitude of the derivative of the converged solution norm curve with respect to log α.

signal-to-noise ratio (SNR) across all collected samples is 20 dB, unless otherwise specified.

B. REGULARIZATION PARAMETERS

To form a faithful image, we require a strategy for choosing the parameters α and β in (9). Common strategies from the literature often choose regularization parameters by analyzing the behavior of the solution and residual. These include the L-curve method, which involves finding a compromise between the solution and residual norms, and generalized

cross-validation (GCV), which involves minimizing a function of the residual and the system inverse matrix [41]. Multiple-parameter versions of these techniques that have some increased complexity have also been presented in the literature (e.g., [42]). For this study, we developed a distinct strategy that is based on our empirical observations of the behavior of the PE-LSM solution norm and that is straightforward to implement. We detail this strategy in this section and then use it for choosing α and β for all results in subsequent sections.

We have made the following empirical observations of the PE-LSM, which are related to but not identical to the observations made for PDFV regularization in [29]. First, while holding β/α constant and sweeping over either α or β, good image quality is typically achieved near an inflection point that marks the transition between large and small solution norms. Second, using large ratios β/α is also beneficial to image quality, as this puts a large emphasis on the PDFV regularization term in (9), which is one of the mechanisms for improving fidelity in our formulation. As will be seen, the PE-LSM demonstrates convergent behavior as β/α increases, which is distinct from non-beamformed PDFV-LSM behavior.

Our regularization heuristic is thus to choose α and β such that the solution norm has converged in β/α and is at an inflection point in the solution norm. We choose to define convergence via a less than 1% change in solution norm across an order of magnitude change in β/α and we define the inflection point via the peak in the derivative of the solution norm with regards to α. We demonstrate our procedure in the following numerical example.

We choose the kite-shaped target shown in Figure 1 and the 360° aperture. We distribute a coarse 5×5 grid of pixel locations across a region of dimension 5×5 m in the imaging domain. We then sweep log α from -8 to 4 in steps of 0.25. For each choice of log α, we sweep $\log(\beta/\alpha)$ from 1 to 6. For every combination of α and β, we apply the PE-LSM via (8), record the solution norms, and then compute the following summation of the norms over the pixels and frequency samples:

$$\eta(\alpha, \beta/\alpha) = \eta_0 \left(\int \int \|\mathbf{g}(k, \mathbf{r}, \alpha, \beta/\alpha)\|^2 d\mathbf{r} dk \right)^{1/2}, \quad (11)$$

where η_0 is a normalization constant such that $\eta = 1$ for the lowest choice of log α. The purpose of computing the summation of norms (11) is to allow us to evaluate the effects of α and β on the solution norm so that we can choose the regularization parameters to satisfy our heuristic.

For illustrative purposes, we plot the solution norm η as a function of log α in Figure 3a. The points form a family of curves defined by $\log(\beta/\alpha)$. For each choice of $\log(\beta/\alpha)$, the solution norm begins at a high value for low log α, stays nearly constant as α increases by multiple orders of magnitude, and then transitions to a region of decreasing solution norm.
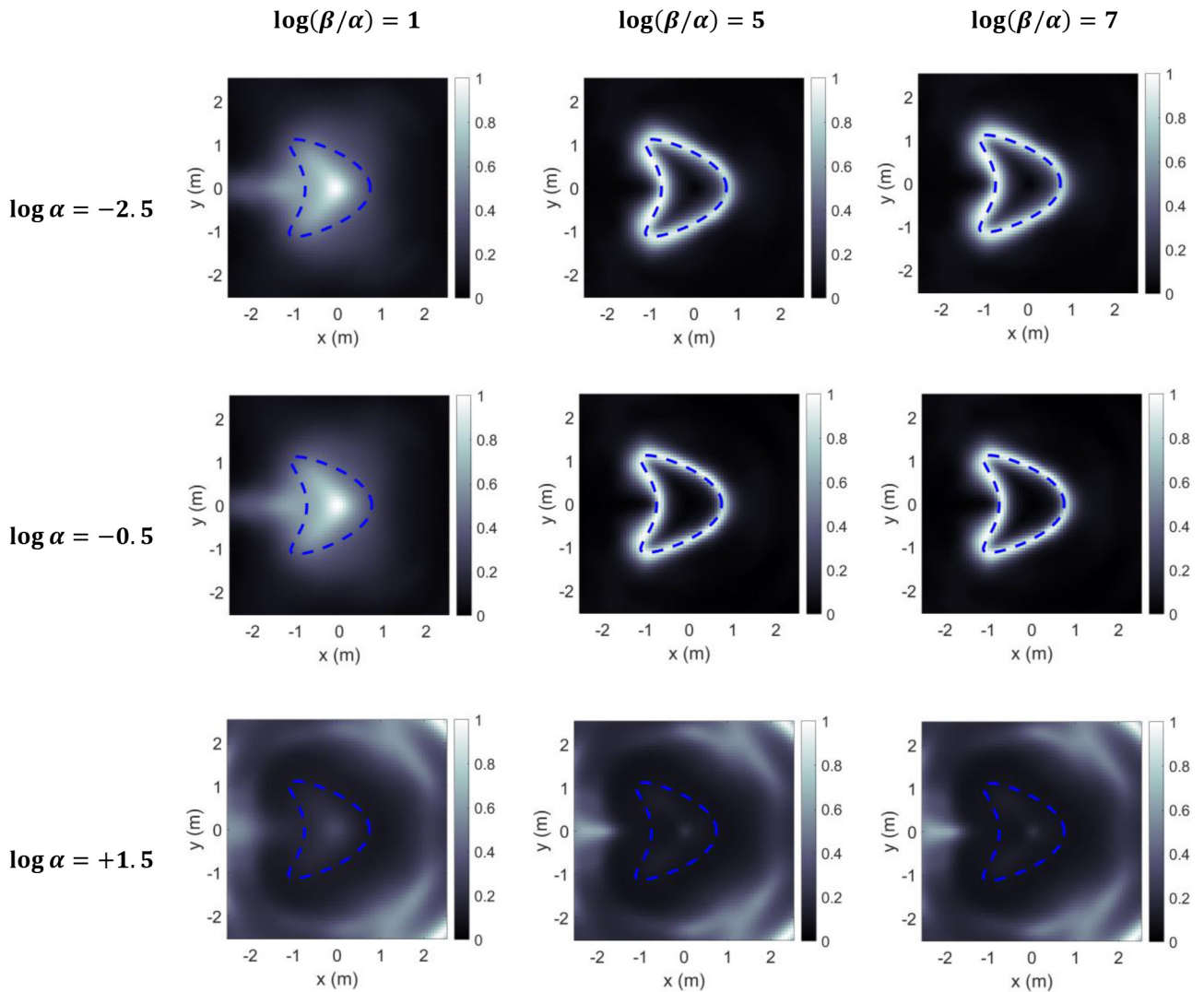
FIGURE 4. PE-LSM imagery for the simulated kite target for various choices of regularization parameters. The aperture angular extent is 360°. The image are normalized such that the most intense pixel has an indicator function value of 1.

To determine which parameters satisfy the heuristic, we first determine which values of $\log(\beta/\alpha)$ cause the solution norm curves to converge. We determine this point of convergence quantitatively by plotting in Figure 3b the percent change in each curve as a function of $\log(\beta/\alpha)$. We define the percent change of the curve at the mth choice of $\log(\beta/\alpha)$ as

$$\nu_m = 100 \times \frac{|\mu_m - \mu_{m-1}|}{\mu_{m-1}}, \tag{12}$$

where

$$\mu_m = \left\{ \int \eta^2\left(\alpha, [\beta/\alpha]_m\right) d\alpha \right\}^{1/2} \tag{13}$$

and $[\beta/\alpha]_m$ is the mth choice for the ratio between the regularization parameters. Our heuristic is satisfied for $\log(\beta/\alpha) = 5$, at which point the percent change falls below 1%.

Next, for the chosen value of $\log(\beta/\alpha) = 5$, we determine which value of α is near the inflection point of the solution norm curve. We select the converged η curve at $\log(\beta/\alpha) = 5$ and plot its derivative with respect to α in Figure 3c. Our heuristic is satisfied at $\log \alpha = -0.5$, where the derivative achieves a clear maximum.

We demonstrate the effectiveness of the heuristic by plotting imaging results for different regularization parameter choices in Figure 4. We form the solution on a finer 70×70 cell, 2.5×2.5 m grid of pixels. We then plot the indicator function from (6). We normalize each image such that the most intense pixel has an indicator function value of 1. The PE-LSM image for regularization parameters that conform to the proposed heuristic, i.e., $\log \alpha = -0.5$ and $\log(\beta/\alpha) = 5$ is of good fidelity to the true target surface. In contrast, decreasing $\log(\beta/\alpha)$ to 1 significantly lowers the definition of the image and increasing $\log \alpha$ to 1.5 results in a total loss of fidelity.
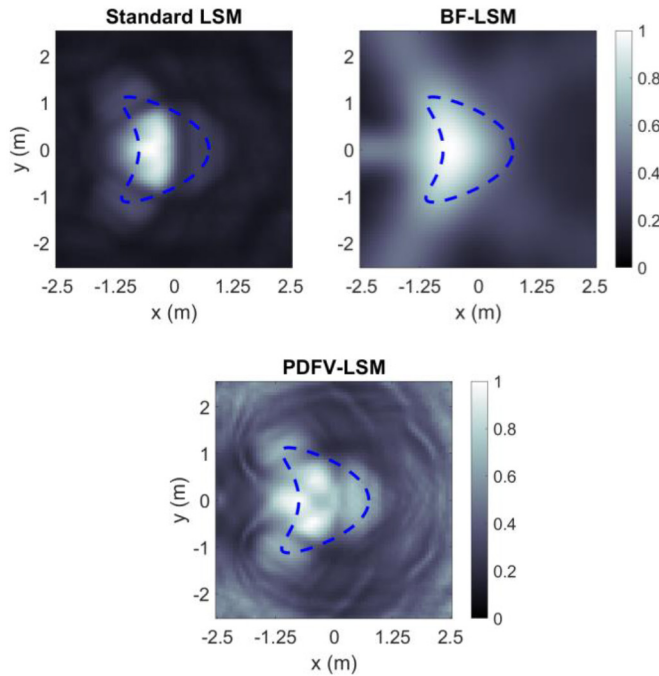
FIGURE 5. Standard LSM, BF-LSM, and PDFV-LSM images of the kite target for comparison with the PE-LSM images of the previous two figures. The aperture angular extent is 360°. The image are normalized such that the most intense pixel has an indicator function value of 1.

C. COMPUTATION OF OTHER LSM VARIANTS FOR COMPARISON

To evaluate the relative performance of the PE-LSM, we compare it to the standard LSM as well as the LSM with either the receive or transmit phase encoding included, but not both. The standard LSM solution is computed via the conventional Tikhonov formulation in (4). The LSM solution with only the receive encoding included, which we will refer to here as the beamforming LSM (BF-LSM) for convenience, is computed via

$$\min_{\mathbf{g}(k,\mathbf{r})} \sum_i \left| \mathbf{w}^{\mathrm{H}}(k_i, \mathbf{r})\boldsymbol{\rho}(k_i, \mathbf{r}) \right|^2 + \alpha \|\mathbf{g}(k_i, \mathbf{r})\|^2, \quad (14)$$

in which the receive beamforming enhancement has been applied to the residual but the PDFV penalty from (9) is not included. Lastly, the LSM solution with only the transmit encoding, which we refer to as the PDFV-LSM as in [29], is computed via

$$\min_{\mathbf{g}(k,\mathbf{r})} \sum_i \|\boldsymbol{\rho}(k_i, \mathbf{r})\|^2 + \alpha \|\mathbf{g}(k_i, \mathbf{r})\|^2 + \beta \|\boldsymbol{\gamma}(k_i, \mathbf{r})\|^2, \quad (15)$$

where the PDFV constraint is included but the beamforming enhancement is not applied to the residual. In each case, we compute the solution across the same multiple-frequency dataset and compute the multifrequency indicator function (6).

We apply these three LSM variants to the example from the previous section. In each case, we sweep the regularization parameters over a large range and choose the α and β

which result in the image of highest fidelity. For the standard LSM and BF-LSM images, the sweep over log α was from -8 to 2 in steps of 1. For the PDFV-LSM, the sweep over log α was -7 to -1 in steps of 2 and the sweep over log(β/α) was from 0 to 8 in steps of 2.

The results are plotted in Figure 5. For each LSM variant, the indicator function is at least somewhat concentrated in the true target footprint. However, the true shape of the target is not clearly evident in any of the images. In the standard LSM image, only the left portion of target is reconstructed at a high indicator level and the curves of the surfaces of the target are not well-resolved. Notably, adding either the beamforming enhancement or the PDFV penalty individually do not appear to obviously improve upon the quality of the standard LSM image. The beamforming enhancement lowers the contrast between the target space and the background without significantly improving the shape of the target reconstruction. The PDFV penalty also reduces the contrast while adding additional interference patterns in the background. This result suggests that, while the PDFV-LSM is effective in the challenging dense-transmit, sparse-receive geometries of [29], it is less effective in the multistatic synthetic aperture geometries of interest in this study. Conversely, the results in the previous section suggest that using the beamforming enhancement and the PDFV penalty in concert via the PE-LSM can significantly improve upon standard LSM processing, assuming that regularization parameters are chosen according to the proposed heuristic, as in the center image in Figure 4.

D. RESULTS FOR A VARIETY OF SIMULATED TARGETS
1) FULL-APERTURE RESULTS

In this section, we evaluate performance of the proposed technique across a wider variety of simulated targets. First, we again consider the case of a 360° synthetic aperture. Results for this scenario are plotted in Figure 6 for four distinct complex targets. For each target, we plot both the PE-LSM image and the standard LSM image. We choose regularization parameters for the PE-LSM for each example according to the heuristic-based procedure described in Section III-B. We choose the regularization parameter for the standard LSM for each example using the same procedure as in Section III-C, i.e., we sweep over a wide range of log α and plot the image that demonstrates the highest visual fidelity. For brevity, we choose not to plot BF-LSM and PDFV-LSM images, as they do not evince significant visual improvement compared to the standard LSM, as in Figure 5.

Figure 6a shows results for a target in the form of a block with two wells of different depths that we refer to as the "key" target. The PE-LSM image demonstrates good fidelity to the complex shape of the target, including the locations and depths of the two wells. In comparison, the standard LSM image gives a poor representation of the true target shape, in that regions of elevated indicator form are not
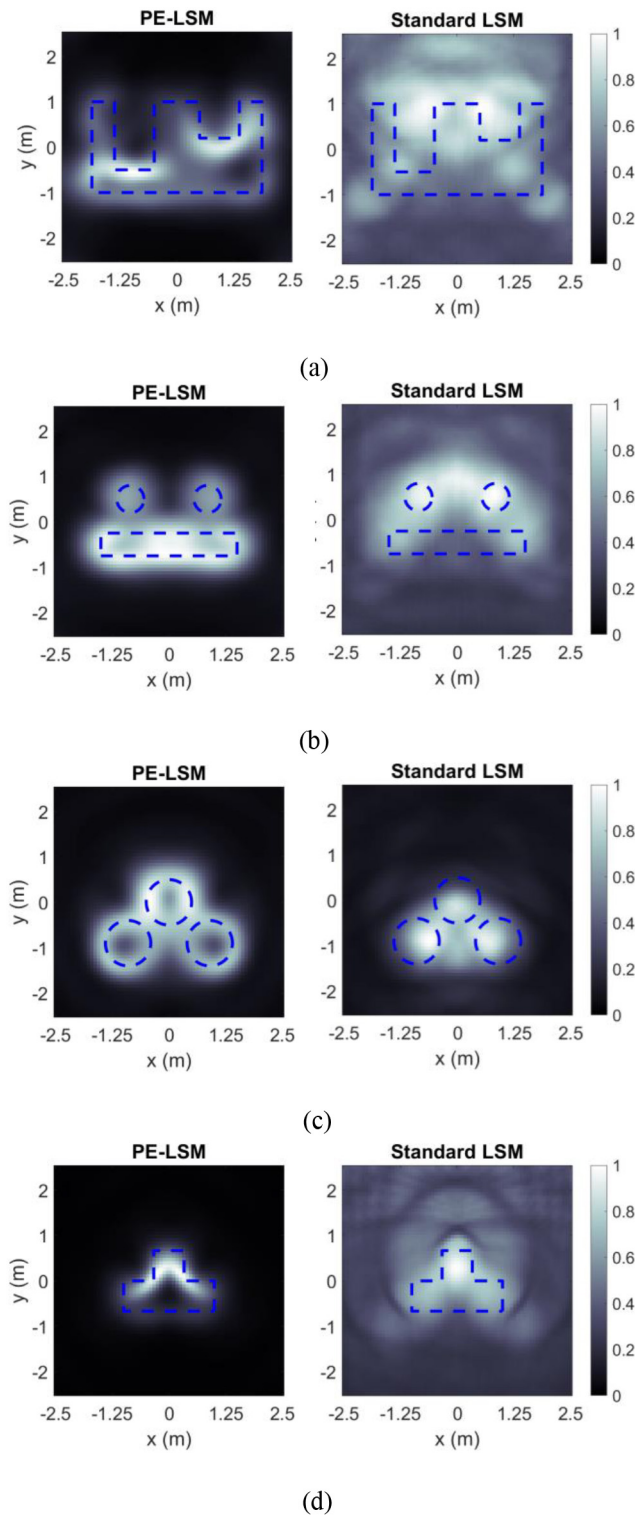
(a)

(b)

(c)

(d)

FIGURE 6. PE-LSM and standard LSM images for a variety of simulated targets. The aperture angular extent is 360°. The image are normalized such that the most intense pixel has an indicator function value of 1.

constricted to the target footprint. In fact, the highest levels of indicator function occur at the openings of the wells.

Figure 6b shows results for a target comprising a horizontal bar and two discs that we refer to as the "jack" target. The PE-LSM image is again of good fidelity, as the reconstructed footprint of each of the three target elements is distinguishable and accurate in terms of location and shape, The standard LSM image is again a poor representation of the true target. The shape of none of the three target elements is distinguishable. The horizontal bar is not reconstructed at all, while the region of high indicator function covers an area that encompasses both discs as well as a significant portion of non-target space.

Figure 6c shows results for a three-disc target formation. In the PE-LSM image, each disc is distinguishable and accurately reconstructed in shape and location. The standard LSM image shows some limited fidelity in that the region of high indicator function is concentrated on the three-disc formation. However, the three discs are not as easily distinguishable compared to the PE-LSM image.

Lastly, Figure 6d shows results for an inverted T-shaped target. In the PE-LSM image, the regions of highest indicator function are concentrated in the vertical bar of the target. The indicator function values in the horizontal bar of the target are lower, but are still higher than the values in non-target space remote from the target. The higher indicator function values for the vertical bar of the target are most likely caused by high-amplitude reflections that are expected from the two dihedral shapes formed at the junction of the vertical and horizontal bars. Still, the PE-LSM demonstrates a significant degree of fidelity to the true target. In comparison, the standard LSM image is of significantly lower fidelity. It evinces a lower contrast between target and non-target space as well as significant interference patterns that make the true target shape much more difficult to discern.

2) LIMITED-APERTURE RESULTS

Next, we consider the more challenging limited-aperture case. In Figure 7, we plot PE-LSM and standard LSM results for the same four targets in the scenario where the synthetic aperture angular extent is only 90°. As illustrated in Figure 1, the aperture is centered on the $+y$-axis.

Across the four targets, the PE-LSM reconstructs the illuminated target surfaces (that is, surfaces facing the synthetic aperture at the top of the targets) with good fidelity. The standard LSM results in Figure 7 are by comparison of much lower quality than the PE-LSM results for each target. The key and jack target standard reconstructions are aberrant to an extent similar to the corresponding standard LSM images from the full-aperture geometry in Figure 6 and show high indicator values in regions that should be empty, such as above the cavities in the key target. The three-disc target image in Figure 7c has lost the somewhat limited fidelity from the standard LSM image in Figure 6c in that the target response is severely elongated in the range direction (i.e., the $-y$-direction) of the array. The standard LSM image of the T-shaped target is also smeared in the range direction.

The results in Figure 7 demonstrate that the PE-LSM can reconstruct a significant degree of the illuminated target geometry from limited aperture scenarios, while the
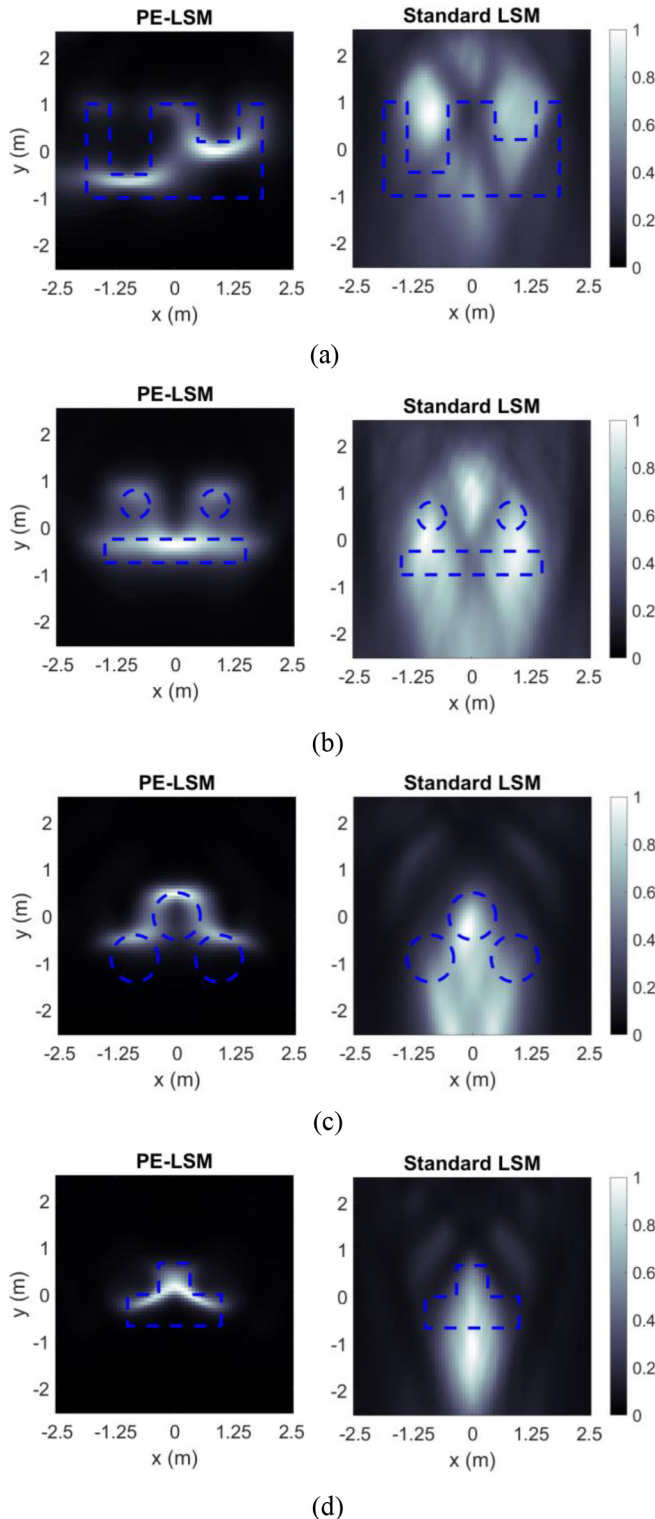
(a)

(b)

(c)

(d)

FIGURE 7. PE-LSM and standard LSM images from a limited aperture for a variety of simulated targets. The aperture is centered on the +y-axis and has an extent of 90°, and thus only the top surfaces are illuminated. The image are normalized such that the most intense pixel has an indicator function value of 1.

performance of the standard LSM is much more aberrant. This outcome demonstrates the ability of the receive and transmit phase encoding of the PE-LSM to leverage range
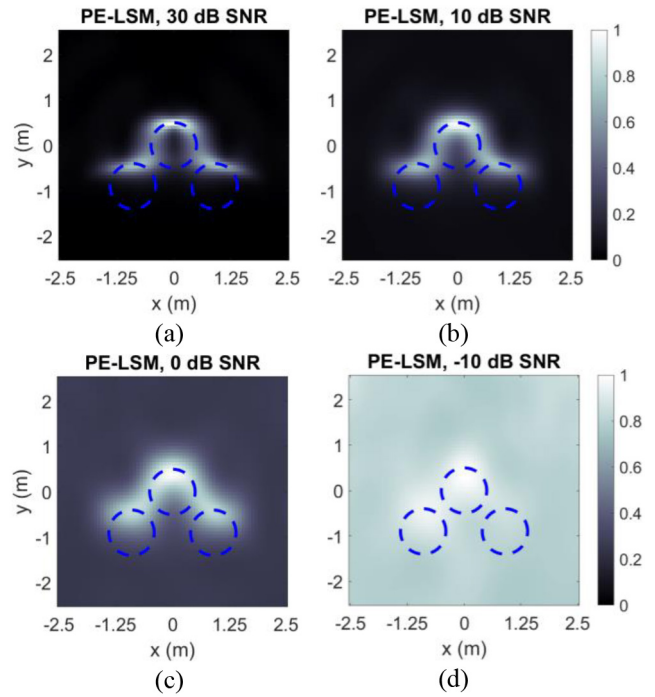

(a)   (b)

(c)   (d)

FIGURE 8. Limited-aperture PE-LSM images for varying SNR. The aperture is centered on the +y-axis and has an extent of 90°. The image are normalized such that the most intense pixel has an indicator function value of 1.

information embedded in the phase of the scattered field. In contrast, the standard LSM lacks such a mechanism, as discussed in Section I, and therefore generates less faithful imagery.

E. EFFECTS OF NOISE

Here, we evaluate the effects of differing levels of noise on the PE-LSM reconstruction. We once again use the limited-aperture geometry from Section III-D and the three-disc target. We generate PE-LSM images for SNRs of 30, 10, 0, and −10 dB in order to compare them to the 20 dB SNR example in Figure 7c. The results are plotted in Figure 8.

The 30 dB SNR image in Figure 8a is virtually identical to the 20 dB SNR example in Figure 7c and thus shows good fidelity to the illuminated target surfaces. The 10 dB SNR image in Figure 8b shows similar levels of fidelity. In the 0 dB SNR image in Figure 8c, the indicator function is still highest along the illuminated surfaces, but the contrast is reduced significantly. In the −10 dB SNR image in Figure 8d, there is little to no contrast between the target and background such that the target shape cannot be easily discerned. Overall, the images in Figure 8 indicate that the PE-LSM is reasonably robust to noise.

F. EFFECTS OF LOWER CONDUCTIVITY

The primary intended use for the PE-LSM is for conducting targets. However, the effects of lower conductivity on the PE-LSM performance are interesting for evaluating the robustness of the technique, and thus are evaluated here for the limited aspect case.

We once again use the limited-aperture geometry and the three-disc target. We set the dielectric constant of the target to 2 and replace the copper-like conductivity with a series of lower conductivities ranging from 20 to 0 mS/m. The results are plotted in Figure 9.

The 20 mS/m image is very similar to Figure 7c, and thus demonstrates good fidelity to the true illuminated target surfaces. The 10 mS/m image also shows good fidelity, although very faint sidelobe-like features appear in the upper half of the image.

In the 5 mS/m image, several arcs of higher indicator function appear in the bottom half of the image. In the 0 mS/m image, these arcs in the bottom half of the image become the most intense features of image, while the indicator values of the top surfaces of the target are greatly reduced. In Figure 9d, there is clearly one spurious arc for each of the three discs.

The explanation for the arcs in the bottom half of the images in Figure 9c and Figure 9d is the set of internal reflections from the bottom surfaces of the three discs. As conductivity is decreased, the targets become more penetrable. Significant reflections therefore originate not only from the illuminated top surfaces of the target, but also from incident waves that penetrate the discs, reflect off of the discs' bottom surfaces, and then exit the discs and return to the receivers. However, the locations of the resulting target responses in the PE-LSM image are displaced from the true bottom surface locations, as the true electrical length traversed by the transmitted and reflected fields is longer than the electrical length used in the design for the PDFV constraint in (10) as well as the receive beamforming weight in (7), which both assume free-space propagation. Similar spurious scattering centers displaced behind dielectric targets have been observed in previous studies of synthetic aperture radar or time reversal techniques [43], [44].

The results in this section demonstrate two properties of the PE-LSM. The first is that although the primary aim for the PE-LSM is for reconstructing conducting targets, it is also effective at imaging targets that have significant conductivity but are not near-perfect conductors, and thus is reasonably robust to target electrical properties. The second is that although the PE-LSM imagery of very low-loss targets evinces low visual fidelity to the true target geometry, the behavior of the technique in response to such targets is predictable and similar to other widely used techniques.

G. EXPERIMENTAL RESULTS

Lastly, we consider an experimental imaging example. We use a limited-aperture dataset that has been made publicly available by researchers from Georgia Tech University [45]. A diagram of the imaging setup is given in Figure 10. Multistatic data are collected by an array of two transmitters and four receivers that move in formation in the x- and y-directions while maintaining a constant height (i.e., z-coordinate).
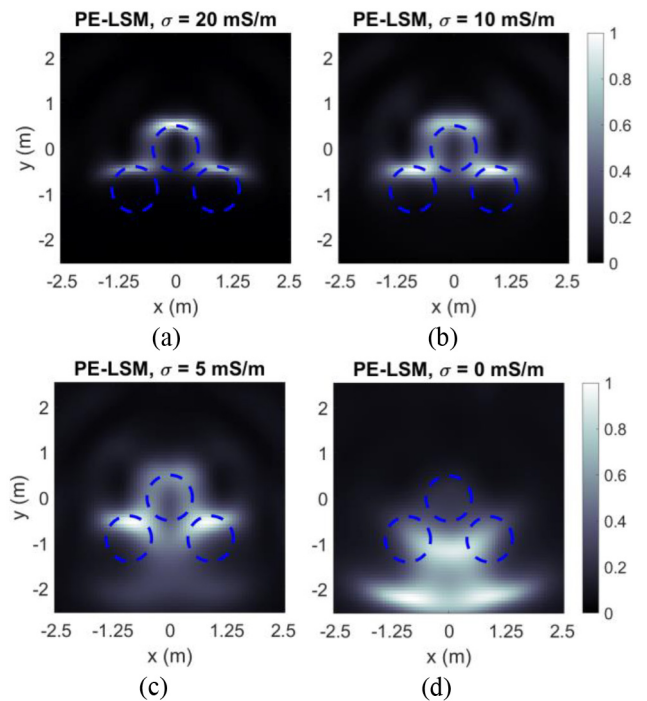

FIGURE 9. Limited-aperture PE-LSM images for varying target conductivity, σ. The aperture is centered on the $+y$-axis and has an extent of 90°. The image are normalized such that the most intense pixel has an indicator function value of 1.
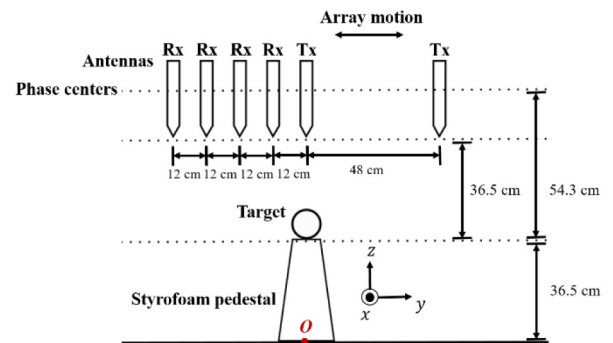

FIGURE 10. The experimental imaging scenario for the Georgia Tech dataset. The '*O*' denotes the origin of the Cartesian coordinate system.

We select data that were collected against a conducting sphere of diameter 11 cm. The sphere rests on a pedestal whose top surface is 54.3 cm below the phase center of the antennas. We set the point on the ground directly beneath the pedestal as the origin of the Cartesian coordinate system defining the imaging geometry.

We select a subset of this dataset such that the array maintains a constant x-coordinate while collecting data across a synthetic aperture in the y-direction. The array undergoes 1.8 m of motion while collecting multistatic samples at 2 cm increments.

The experimental array setup differs from the array presented in Figure 1 in that the transmitters are not centrally located among the receivers, which causes a lack
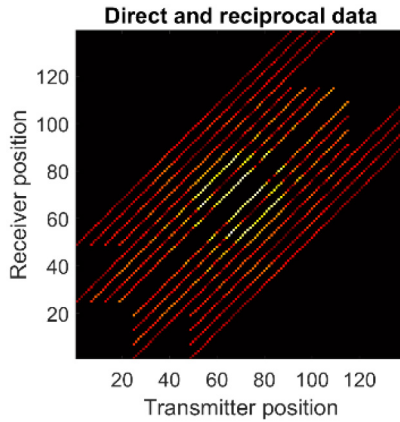
FIGURE 11. The data matrix for imaging the Georgia Tech experimental data, which includes both direct and reciprocal pairs.

of symmetry. We can use this to our advantage by filling in a larger number of samples of the $\mathbf{E}(k)$ matrix than are directly collected using the principle of reciprocity, as in [34], [40]. The resulting data matrix is shown in Figure 11. In the data matrix, the traces below the monostatic diagonal correspond to direct data, and traces above the diagonal correspond to reciprocal data.

We apply both standard LSM and PE-LSM processing to the experimental data. For the standard LSM, faithful imaging is somewhat complicated by the presence of reflections from the ground. To account for this, we adopt a background removal procedure [46] that was also used on the Georgia Tech dataset in a previous conference paper [34]. Within a trace, if we define a sample collected at spatial coordinate y and spatial frequency k as $s(y, k)$, then the data sample after background removal is given by

$$s'(y, k) = s(y, k) - \frac{1}{2L + 1} \sum_{n=-L}^{L} s(y - n\Delta y, k) \quad (16)$$

where Δy is the spatial step and $2L$ is the number of spatial steps in an averaging window. The rationale for this procedure is that the ground reflection is expected to be similar across spatial samples, and thus by subtracting out an average of the data across a spatial window we can mitigate the degree of corruption of the target signal from the ground. In this study, we use $L = 30$ for the standard LSM results, as we have found empirically that decreasing L below this value leads to gradual image degradation and increasing it above this value yields no additional benefit.

We apply the background removal procedure to the standard LSM data by necessity in order to mitigate significant image contamination from the ground reflections. For the PE-LSM images, we do not apply the background removal procedure in order to demonstrate the robustness of the PE-LSM technique to these reflections. Achieving faithful imagery without the background removal step is of interest for avoiding unnecessary computation.

To account for the 3D propagation environment, we modify the Green's function in (3) such that

$$\Phi_0^i(k, \mathbf{r}) = \exp\left(-jkd_{\text{rec}}^i(\mathbf{r})\right) / d_{\text{rec}}^i(\mathbf{r}), \quad (17)$$

which is the conventional Green's function in 3D. We have found that this choice modestly improves the appearance of the standard LSM image.

We form two sets of experimental images. The first uses data from 1-3 GHz, while the second uses data from 2-4 GHz. In both cases, we keep 11 frequencies in the 2 GHz of bandwidth. In Figure 12, we plot the results across a wide imaging scene in order to provide the best comparison with previously published results in [34]. We also plot detail images for a narrower scene surrounding the target in Figure 13. For the $1 - 3$ GHz band, the standard LSM image shows some concentration of indicator function at the target location. The target response extends above the target, and has an overall dimension of approximately 0.2 m. The standard LSM image in Figure 12a is thus consistent with the results for the same frequency band published in [34] for the cross-section parallel to the yz-plane. Similar behavior can be observed in the $2 - 4$ GHz band, with the most noticeable difference being a lowering of contrast between target and non-target space. Across both bands, the standard LSM images display somewhat limited geometric information about the target except for its rough location, with somewhat limited resolution in the range direction (i.e., the z-direction).

In comparison, the PE-LSM images are of better quality. The indicator functions are concentrated along the upper surface of the circular target with significantly better resolution in the range direction. There is somewhat tighter concentration of indicator function in the lateral direction for the $2 - 4$ GHz band, perhaps due to the smaller wavelength in that band. The target contrast does not degrade significantly when the frequency is increased to the $2 - 4$ GHz band, as it does for the standard LSM images.

Thus, the results in Figure 12 and Figure 13 demonstrate effective PE-LSM imaging in an experimental imaging scenario. In a manner similar to the simulated results in Figure 7, they also demonstrate the improved ability of the PE-LSM to reconstruct the illuminated target surface in limited-aperture scenarios as compared to the standard LSM via leveraging range information in the multifrequency signal. The results also demonstrate the relative robustness of the PE-LSM to the reflections from the ground, since no background removal step was needed to achieve the good-fidelity PE-LSM results in Figures 12 and 13. This robustness may be due to spatial filtering effects of the PDFV constraint and the beamforming enhancement.

H. DISCUSSION
The results in Sections III-B–III-G demonstrate consistent and significant improvement to the fidelity of the reconstruction of the target illuminated surfaces when using
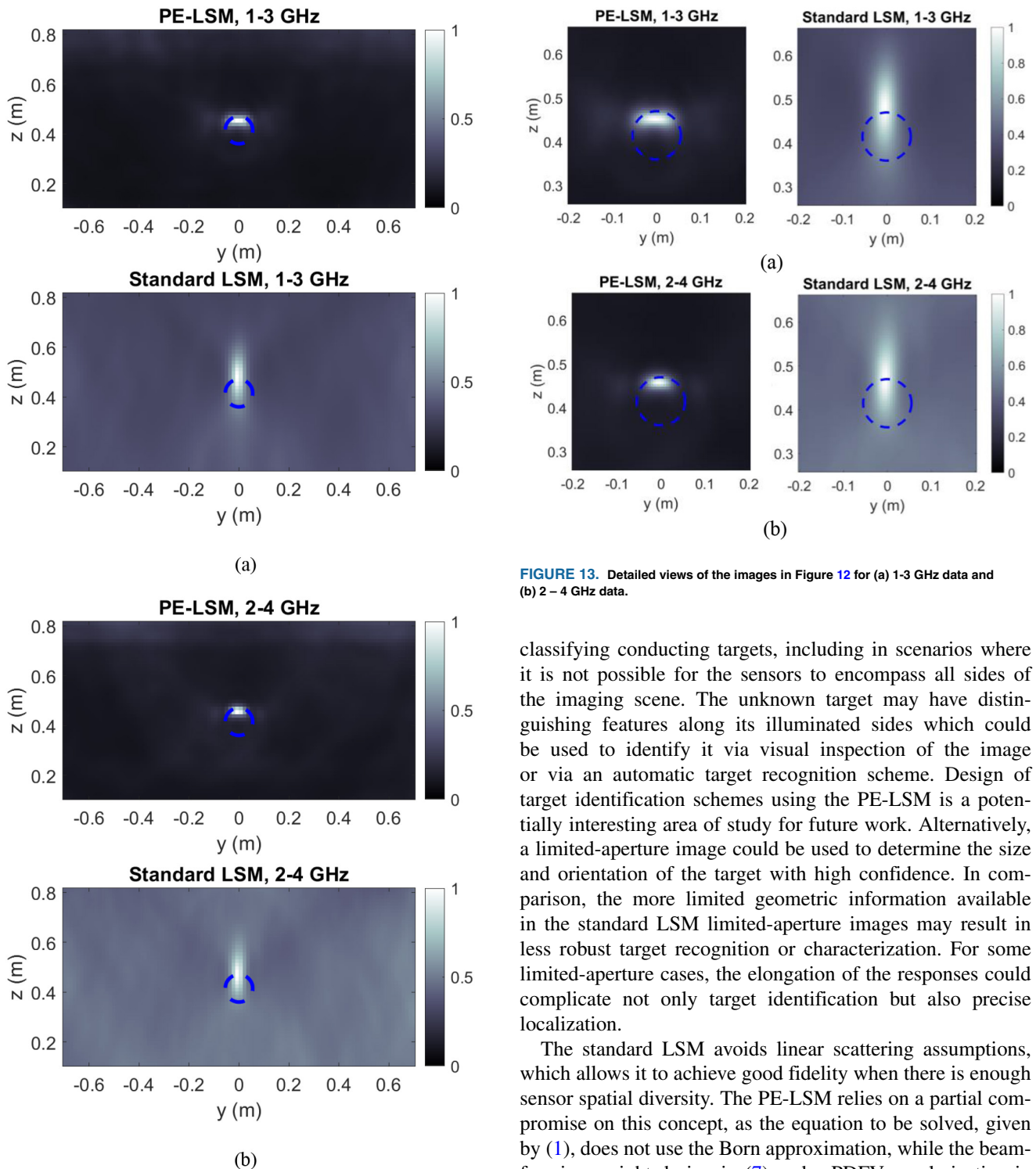
(a)

(b)

FIGURE 12. Limited-aperture PE-LSM and Standard LSM images for the experimental data against an 11-cm conducting sphere. (a) Images formed from 1-3 GHz data. (b) Images formed from 2-4 GHz data. The aperture is above the target, and thus only the top surface of the target is illuminated. The image are normalized such that the most intense pixel has an indicator function value of 1.

(a)

(b)

FIGURE 13. Detailed views of the images in Figure 12 for (a) 1-3 GHz data and (b) 2 – 4 GHz data.

classifying conducting targets, including in scenarios where it is not possible for the sensors to encompass all sides of the imaging scene. The unknown target may have distinguishing features along its illuminated sides which could be used to identify it via visual inspection of the image or via an automatic target recognition scheme. Design of target identification schemes using the PE-LSM is a potentially interesting area of study for future work. Alternatively, a limited-aperture image could be used to determine the size and orientation of the target with high confidence. In comparison, the more limited geometric information available in the standard LSM limited-aperture images may result in less robust target recognition or characterization. For some limited-aperture cases, the elongation of the responses could complicate not only target identification but also precise localization.

The standard LSM avoids linear scattering assumptions, which allows it to achieve good fidelity when there is enough sensor spatial diversity. The PE-LSM relies on a partial compromise on this concept, as the equation to be solved, given by (1), does not use the Born approximation, while the beamforming weight design in (7) and a PDFV regularization in (10) do use the Born approximation. As seen in the results in this paper, making this compromise allows for greater flexibility in sensor geometry while achieving several benefits associated with the LSM, namely good fidelity and computation via solving linear systems of equations. Future work may involve enhancing the PE-LSM by using more complex schemes for designing (7) and (10), perhaps by incorporating assumed or estimated target electrical properties. In addition, (7) and (10) could be modified to allow

the PE-LSM as compared to standard Tikhonov-regularized LSM. The good fidelity of the PE-LSM imagery suggests that the PE-LSM could be useful for remotely identifying or

for imaging a target embedded under a penetrable surface by taking into account the expected electrical length of the non-free-space propagation path.

IV. CONCLUSION

In this paper, we introduced a formulation of the LSM which achieves high imaging performance of conducting targets using only a few sensors by encoding propagation-based phase information into the solution. We evaluated the performance of the proposed PE-LSM in challenging scenarios where a small array of sensors collect data across a synthetic aperture. The scenario is interesting due to its potential practicality as well as the challenge it presents to conventional LSM processing due to the relatively narrow range of bistatic angles between the transmitter and receivers. Using a variety of simulated datasets as well as an example experimental dataset, we demonstrated a clear and consistent improvement in imaging performance for the PE-LSM compared to the standard LSM. The improvement is particularly notable for cases using limited apertures and electrically large targets, given the well-known limitations of conventional LSM processing for these factors. Thus, the phase encoding enhancements in the PE-LSM allow for greater flexibility in sensor configuration while achieving several benefits of LSM processing, such as good image fidelity and avoidance of nonlinear optimization.

REFERENCES

[1] Y. M. Wang and W. C. Chew, "An iterative solution of the two-dimensional electromagnetic inverse scattering problem," *Int. J. Imag. Syst. Technol.*, vol. 1, no. 1, pp. 100–108, 1989.

[2] W. C. Chew and Y. M. Wang, "Reconstruction of two-dimensional permittivity distribution using the distorted born iterative method," *IEEE Trans. Med. Imag.*, vol. 9, no. 2, pp. 218–225, Jun. 1990.

[3] A. Abubakar and P. M. van den Berg, "The contrast source inversion method for location and shape reconstructions," *Inverse Problems*, vol. 18, pp. 495–510, Mar. 2002.

[4] R. O. Mays, N. Behdad, and S. C. Hagness, "Array sensitivity for model-based microwave breast imaging," *IEEE Trans. Antennas Propag.*, vol. 65, no. 6, pp. 2958–2965, Jun. 2017.

[5] L. Poli, G. Oliveri, and A. Massa, "Imaging sparse metallic cylinders through a local shape function Bayesian compressive sensing approach," *J. Opt. Soc. America*, vol. 30, no. 6, pp. 1261–1272, 2013.

[6] T. Takenaka, Z. Q. Meng, T. Tanaka, and W. C. Chew, "Local shape function combined with genetic algorithm applied to inverse scattering for strips," *Microw. Opt. Technol. Lett.*, vol. 16, pp. 337–341, Dec. 1997.

[7] G. P. Otto and W. Chew, "Microwave inverse scattering /spl minus/ local shape function imaging for improved resolution of strong scatterers," *IEEE Trans. Microw. Theory Technol.*, vol. 42, no. 1, pp. 137–141, Jan. 1994.

[8] X. Ye, "Electromagnetic imaging of wave impenetrable objects," in *Proc. 11th Eur. Conf. Antennas Propag.*, Paris, France, 2017, pp. 1421–1428.

[9] X. Ye, Y. Zhong, and X. Chen, "Reconstructing perfectly electric conductors by the subspace-based optimization method with continuous variables," *Inverse Problems*, vol. 27, Apr. 2011, Art. no. 55011.

[10] J. Shen, Y. Zhong, X. Chen, and L. Ran, "Inverse scattering problems of reconstructing perfectly electric conductors with TE illumination," *IEEE Trans. Antennas Propag.*, vol. 61, no. 9, pp. 4713–4721, Sep. 2013.

[11] M. Stevanovic, L. Crocco, A. R. Djordjević, and A. Nehorai, "Higher order sparse microwave imaging of PEC scatterers," *IEEE Trans. Antennas Propag.*, vol. 64, no. 3, pp. 988–997, Mar. 2016.

[12] N. Vojnovic, M. N. Stevanovic, L. Crocco, and A. R. Djordjevic, "High-order sparse shape imaging of PEC and dielectric targets using TE polarized fields," *IEEE Trans. Antennas Propag.*, vol. 66, no. 4, pp. 2035–2043, Apr. 2018.

[13] M. M. Nikolic, A. Nehorai, and A. R. Djordjevic, "Electromagnetic imaging of hidden 2-D PEC targets using sparse-signal modeling," *IEEE Trans. Geosci. Remote Sens.*, vol. 51, no. 5, pp. 2707–2721, May 2013.

[14] M. Bevacqua and T. Isernia, "Shape reconstruction via equivalence principles, constrained inverse source problems and sparsity promotion," *Progr. Electromagn. Res.*, vol. 158, pp. 37–48, Feb. 2017.

[15] M. Bevacqua and R. Palmeri, "Qualitative methods for the inverse obstacle problem: A comparison on experimental data," *J. Imag.*, vol. 5, no. 4, p. 47, 2019.

[16] S. Sun, B. J. Kooij, A. G. Yarovoy, and T. Jin, "A linear method for shape reconstruction based on the generalized multiple measurement vectors model," *IEEE Trans. Antennas Propag.*, vol. 66, no. 4, pp. 2016–2025, Apr. 2018.

[17] F.-F. Wang and Q. H. Liu, "A Bernoulli–Gaussian binary inversion method for high-frequency electromagnetic imaging of metallic reflectors," *IEEE Trans. Antennas Propag.*, vol. 68, no. 4, pp. 3184–3193, Apr. 2020.

[18] F. Soldovieri, A. Brancaccio, G. Leone, and R. Pierri, "Shape reconstruction of perfectly conducting objects by multiview experimental data," *IEEE Trans. Geosci. Remote Sens.*, vol. 43, no. 1, pp. 65–71, Jan. 2005.

[19] R. Solimene, A. Buonanno, F. Soldovieri, and R. Pierri, "Physical optics imaging of 3-D PEC objects: Vector and multipolarized approaches," *IEEE Trans. Geosci. Remote Sens.*, vol. 48, no. 4, pp. 1799–1808, Apr. 2010.

[20] W.-K. Park, "Direct sampling method for retrieving small perfectly conducting cracks," *J. Comput. Phys.*, vol. 373, pp. 648–661, Nov. 2018.

[21] W.-K. Park, "Direct sampling method for anomaly imaging from scattering parameter," *Appl. Math. Lett.*, vol. 18, pp. 63–71, Jul. 2018.

[22] R. Potthast, "A study on orthogonality sampling," *Inverse Problems*, vol. 26, Jul. 2010, Art. no. 74015.

[23] M. T. Bevacqua, T. Isernia, R. Palmeri, M. N. Akinci Jr., and L. Crocco, "Physical insight unveils new imaging capabilities of orthogonality sampling method," *IEEE Trans. Antennas Propag.*, vol. 68, no. 5, pp. 4014–4021, May 2020.

[24] F. Cakoni, D. Colton, and P. Monk, *The Linear Sampling Method in Inverse Scattering Theory*. Philadelphia, PA, USA: Soc. Ind. Appl. Math., 2011.

[25] I. Catapano, L. Crocco, and T. Isernia, "On simple methods for shape reconstruction of unknown scatterers," *IEEE Trans. Antennas Propag.*, vol. 55, no. 5, pp. 1431–1436, May 2007.

[26] K. Agarwal, X. Chen, and Y. Zhong, "A multipole-expansion based linear sampling method for solving inverse scattering problems," *Opt. Exp.*, vol. 18, no. 6, pp. 6366–6381, 2010.

[27] M. Cheney, "The linear sampling method and the MUSIC algorithm," *Inverse Problems*, vol. 17, no. 4, pp. 591–595, 2000.

[28] B. B. Guzina, F. Cakoni, and C. Bellis, "On the multi-frequency obstacle reconstruction via the linear sampling method," *Inverse Problems*, vol. 29, Nov. 2010, Art. no. 125005.

[29] M. J. Burfeindt and H. F. Alqadah, "Qualitative inverse scattering for sparse-aperture data collections using a phase-delay frequency variation constraint," *IEEE Trans. Antennas Propag.*, vol. 68, no. 11, pp. 7530–7540, Nov. 2020.

[30] M. J. Burfeindt and H. F. Alqadah, "Boundary-condition-enhanced linear sampling method imaging of conducting targets from sparse receivers," *IEEE Trans. Antennas Propag.*, vol. 70, no. 3, pp. 2246–2260, Mar. 2022.

[31] M. J. Burfeindt and H. F. Alqadah, "Receive-beamforming-enhanced linear sampling method imaging," in *Proc. IEEE Res. Appl. Photon. Defense (RAPID) Conf.*, 2021, pp. 1–2.

[32] Y. Guo, P. Monk, and D. Colton, "The linear sampling method for sparse small aperture data," *Appl. Anal.*, vol. 95, no. 8, pp. 1599–1615, 2016.

[33] H. Haddar, A. Lechleiter, and S. Marmorat, "An improved time domain linear sampling method for Robin and Neumann obstacles," *Appl. Anal.*, vol. 93, no. 2, pp. 369–390, 2014.

[34] M. Ambrosanio, M. T. Bevacqua, T. Isernia, and V. Pascazio, "Experimental multistatic imaging via the linear sampling method," in *Proc. IEEE Int. Geosci. Remote Sens. Symp.*, 2019, pp. 3586–3589.

[35] L. Audibert and H. Haddar, "The generalized linear sampling method for limited aperture measurements," *SIAM J. Imag. Sci.*, vol. 10, no. 2, pp. 845–870, 2017.

[36] I. Catapano, L. Crocco, and T. Isernia, "Improved sampling methods for shape reconstruction of 3-D buried targets," *IEEE Trans. Geosci. Remote Sens.*, vol. 46, no. 10, pp. 3265–3273, Oct. 2008.

[37] M. T. Bevacqua, S. Di Meo, L. Crocco, T. Isernia, and M. Pasian, "Millimeter-waves breast cancer imaging via inverse scattering techniques," *IEEE J. Electromagn. RF Microw. Med. Biol.*, vol. 5, no. 3, pp. 246–253, Sep. 2021.

[38] I. Catapano, F. Soldovieri, and L. Crocco, "On the feasibility of the linear sampling method for 3D GPR surveys," *Progr. Electromagn. Res.*, vol. 118, pp. 185–203, Jul. 2011.

[39] H. F. Alqadah, "Multi-frequency LSM for buried object detection," in *Proc. Int. Conf. Electromagn. Adv. Appl. (ICEAA)*, 2017, pp. 1323–1326.

[40] M. Ambrosanio, M. T. Bevacqua, T. Isernia, and V. Pascazio, "Performance analysis of tomographic methods against experimental contactless multistatic ground penetrating radar," *IEEE J. Sel. Topics Appl. Earth Observ. Remote Sens.*, vol. 14, pp. 1171–1183, Oct. 2020.

[41] P. C. Hansen, *Rank-Deficient and Discrete Ill-Posed Problems.* Philadelphia, PA, USA: Soc. Ind. Appl. Math., 1998.

[42] C. Brezinski, M. Redivo-Zaglia, G. Rodriguez, and S. Seatzu, "Multi-parameter regularization techniques for ill-conditioned linear systems," *Numer. Math.*, vol. 94, pp. 203–228, Apr. 2003.

[43] C.-S. Ku, K.-S. Chen, P.-C. Chang, and Y.-L. Chang, "Imaging simulation for synthetic aperture radar: A full-wave approach," *Remote Sens.*, vol. 10, no. 9, p. 1404, 2018.

[44] A. Cresp, I. Aliferis, M. J. Yedlin, C. Pichot, and J.-Y. Dauvignac, "Investigation of time-reversal processing for surface-penetrating radar detection in a multiple-target configuration," in *Proc. Eur. Radar Conf.*, 2008, pp. 144–147.

[45] T. Counts, A. C. Gurbuz, W. R. Scott Jr., J. H. McClellan, and K. Kim, "Multistatic ground-penetrating radar experiments," *IEEE Trans. Geosci. Remote Sens.*, vol. 45, no. 8, pp. 2544–2553, Aug. 2007.

[46] R. Persico, *Introduction to Ground Penetrating Radar: Inverse Scattering and Data Processing.* Hoboken, NJ, USA: Wiley, 2014.